The Astrophysical Journal Letters, 1004:L37 (15pp), 2026 June 20 https://doi.org/10.3847/2041-8213/ae734e

The Transitional Type Ibn/IIn SN 2022pda, with Pre-explosion Outbursts and a Double-peaked Light Curve

Y.-Z. Cai (蔡永志)[1,2], A. Pastorello[2], R. Chiba[3,4], T. J. Moriya[3,4,5], A. Reguitti[2,6], L. Tartaglia[7], S. Moran[8,9], S. Campana[6], Z.-Y. Wang[10,11], J.-W. Zhao[12,13], J. P. Anderson[14], S. Benetti[2], S. J. Brennan[15], E. Cappellaro[2], K. C. Chambers[16], T.-W. Chen[17], Z.-H. Chen[18], T. de Boer[19], Y.-Z. Dong[20,21], J. Duarte[22], N. Elias-Rosa[2,23], M. Fraser[24], W.-P. Gan[25], H. Gao[19], M. Gromadzki[26], G. Hosseinzadeh[27], D. A. Howell[28,29], C. Inserra[30], T. Kangas[31,32], E. Kankare[8], T. Kravtsov[8,31], L.-P. Li[1], C.-C. Lin[19], T. B. Lowe[19], P. Lundqvist[33], E. A. Magnier[19], K. Matilainen[8], P. A. Mazzali[34,35], C. McCully[28], P. Minguez[36], T. E. Müller-Bravo[37,38], M. Newsome[28,29,39], E. Padilla Gonzalez[28,29], C. Pellegrino[28,29], P. J. Pessi[40], T. Petrushevska[41], G. Pignata[42], R. P. Santos[14,22], S. Schulze[43,44], S. J. Smartt[45,46], I. A. Smith[47], K. W. Smith[45,46], J. Sollerman[33], S. Srivastav[46,48], M. D. Stritzinger[49], G. Terreran[50], G. Valerin[2], R. Wainscoat[19], S.-Q. Wang (王善钦)[51], D. R. Young[46], L. Galbany[23,52], Z. Li[1], I. Salmaso[2,53], S. Zha (查帅)[1], J.-M. Bai (白金明)[1], B. Wang (王博)[1], X.-F. Wang (王晓锋)[18,54], and J.-J. Zhang (张居甲)[1]

[1] International Centre of Supernovae (ICESUN), Yunnan Key Laboratory of Supernova Research, Yunnan Observatories, Chinese Academy of Sciences (CAS), Kunming 650216, People's Republic of China; yongzhi.cai@inaf.it, jujia@ynao.ac.cn
[2] INAF—Osservatorio Astronomico di Padova, Vicolo dell'Osservatorio 5, 35122 Padova, Italy
[3] Graduate Institute for Advanced Studies, SOKENDAI, 2-21-1 Osawa, Mitaka, Tokyo 181-8588, Japan
[4] National Astronomical Observatory of Japan, National Institutes of Natural Sciences, 2-21-1 Osawa, Mitaka, Tokyo 181-8588, Japan
[5] School of Physics and Astronomy, Monash University, Clayton, Victoria 3800, Australia
[6] INAF—Osservatorio Astronomico di Brera, Via Bianchi 46, 23807, Merate (LC), Italy
[7] INAF—Osservatorio Astronomico d'Abruzzo, via Mentore Maggini, s.n.c. I-64100 Teramo, Italy
[8] Department of Physics and Astronomy, University of Turku, FI-20014 Turku, Finland
[9] School of Physics and Astronomy, University of Leicester, University Road, Leicester LE1 7RH, UK
[10] School of Physics and Astronomy, Beijing Normal University, Beijing 100875, People's Republic of China
[11] Department of Physics, Faculty of Arts and Sciences, Beijing Normal University, Zhuhai 519087, People's Republic of China
[12] South-Western Institute for Astronomy Research, Yunnan University, Kunming 650500, People's Republic of China
[13] Yunnan Key Laboratory of Survey Science, Yunnan University, Kunming, Yunnan 650500, People's Republic of China
[14] European Southern Observatory, Alonso de Córdova 3107, Vitacura, Casilla 19001, Santiago, Chile
[15] Max Planck Institute for Extraterrestrial Physics, Max-Planck-Gesellschaft, Giessenbachstraße 1, Garching, 85748, Germany
[16] Institute for Astronomy, University of Hawaii, 2680 Woodlawn Drive, Honolulu, HI 96822, USA
[17] Graduate Institute of Astronomy, National Central University, 300 Jhongda Road, 32001, Jhongli, Taiwan
[18] Physics Department, Tsinghua University, Beijing 100084, People's Republic of China; wang_xf@mail.tsinghua.edu.cn
[19] Institute for Astronomy, University of Hawai'i, 2680 Woodlawn Drive, Honolulu, HI 96822, USA
[20] Center for Astrophysics — Harvard & Smithsonian, Cambridge, MA 02138, USA
[21] The NSF AI Institute for Artificial Intelligence and Fundamental Interactions, USA
[22] CENTRA, Instituto Superior Técnico, Universidade de Lisboa, Av. Rovisco Pais 1, 1049-001 Lisboa, Portugal
[23] Institute of Space Sciences (ICE, CSIC), Campus UAB, Carrer de Can Magrans, s/n, E-08193 Barcelona, Spain
[24] School of Physics, O'Brien Centre for Science North, University College Dublin, Belfield, Dublin 4, Ireland
[25] Nanjing Hopes Technology Co., Ltd. Nanjing, 210000, People's Republic of China
[26] Astronomical Observatory, University of Warsaw, Al. Ujazdowskie 4, 00-478 Warszawa, Poland
[27] Steward Observatory, University of Arizona, 933 North Cherry Avenue, Tucson, AZ 85721-0065, USA
[28] Las Cumbres Observatory, 6740 Cortona Drive, Suite 102, Goleta, CA 93117, USA
[29] Department of Physics, University of California, Santa Barbara, Santa Barbara, CA 93106, USA
[30] Cardiff Hub for Astrophysics Research and Technology, School of Physics & Astronomy, Cardiff University, Queens Buildings, The Parade, Cardiff, CF24 3AA, UK
[31] Finnish Centre for Astronomy with ESO (FINCA), University of Turku, Vesilinnantie 5, Quantum 20014 Turku, Finland
[32] Tuorla Observatory, Department of Physics and Astronomy, University of Turku, 20014Turku, Finland
[33] The Oskar Klein Centre, Department of Astronomy, Stockholm University, AlbaNova, SE-10691 Stockholm, Sweden
[34] Astrophysics Research Institute, Liverpool John Moores University, Liverpool Science Park, 146 Brownlow Hill, Liverpool L3 5RF, UK
[35] Max-Planck-Institut für Astrophysik, Karl-Schwarzschild Str. 1, D-85741 Garching, Germany
[36] Research Corporation of the University of Hawai'i, 2680 Woodlawn Drive, Honolulu, HI 96822, USA
[37] School of Physics, Trinity College Dublin, The University of Dublin, Dublin 2, Ireland
[38] Instituto de Ciencias Exactas y Naturales (ICEN), Universidad Arturo Prat, Chile
[39] Department of Astronomy, The University of Texas at Austin, 2515 Speedway, Stop C1400, Austin, TX 78712, USA
[40] Astrophysics Division, National Centre for Nuclear Research, Pasteura 7, 02-093 Warsaw, Poland
[41] Center for Astrophysics and Cosmology, University of Nova Gorica, Vipavska 11c, 5270 Ajdovščina, Slovenia
[42] Instituto de Alta Investigaciòn, Universidad de Tarapacà, Casilla 7D, Arica, Chile
[43] Center for Interdisciplinary Exploration and Research in Astrophysics (CIERA), NorthwesternUniversity, Evanston, IL, USA
[44] The Oskar Klein Centre, Department of Physics, StockholmUniversity, AlbaNova University Center, Stockholm, Sweden
[45] Department of Physics, University of Oxford, Denys Wilkinson Building, Keble Road, Oxford OX1 3RH, UK
[46] Astrophysics Research Centre, School of Mathematics and Physics, Queen's University Belfast, Belfast BT7 1NN, UK
[47] Institute for Astronomy, University of Hawai'i, 34 Ohia Ku Street, Pukalani, HI 96768-8288, USA
[48] Astrophysics sub-Department, Department of Physics, University of Oxford, Keble Road, Oxford, OX1 3RH, UK
[49] Department of Physics and Astronomy, Aarhus University, Ny Munkegade 120, DK-8000 Aarhus C, Denmark
[50] Adler Planetarium, 1300 S. DuSable Lake Shore Drive, Chicago, IL 60605, USA
[51] Guangxi Key Laboratory for Relativistic Astrophysics, School of Physical Science and Technology, Guangxi University, Nanning 530004, People's Republic of China
[52] Institut d'Estudis Espacials de Catalunya (IEEC), E-08034 Barcelona, Spain

[53] INAF—Osservatorio Astronomico di Capodimonte, Salita Moiariello 16, 80131 Napoli, Italy
[54] Purple mountain observatory, Chinese Academy of Sciences, Nanjing 210023, People's Republic of China
Received 2026 May 5; revised 2026 May 22; accepted 2026 May 23; published 2026 June 22

Abstract

We report the results of a photometric and spectroscopic follow-up campaign of the unusual interacting supernova (SN) 2022pda. Precursor variability lasting ∼100 days is observed before the explosion. The SN light curve has a double-peak shape. It reached a first maximum of $M_r = -19.6 \pm 0.2$ mag, followed by an initial 2 month decline and a second, broad peak lasting about 6 months. The early spectra show a blue continuum with dominant H and He emission lines. A high-resolution pre-maximum spectrum shows that the profile of the He I λ 5876 line consists of a moderately narrow (∼1900 km s^{-1}) P Cygni absorption superposed on a broader (∼3300 km s^{-1}) component. In the blue region, several spectral features are identified, including C III/N III/O II blends. Two broad bumps at 4600–5200 Å and 6400–6800 Å regions reveal a complex profile, which are likely due to blends of H, He, and other emission lines. Late-time spectra are still dominated by prominent and broad H and He lines in emission. Shock-driven model fits to the bolometric light curve suggest that the SN is powered by interaction with a massive CSM with enhanced mass-loss rates ∼5 $M_\odot$yr^{-1}, expelled during two events that occurred ∼1 and ∼0.2 yr before the explosion. The overall SN evolution indicates that SN 2022pda is a transitional event between an H-rich SN IIn (SN 2009ip-like) and an He-rich SN Ibn. Our findings suggest that the progenitor was likely a luminous blue variable transitioning towards a Wolf–Rayet stage.

Unified Astronomy Thesaurus concepts: Supernovae (1668); Core-collapse supernovae (304); Circumstellar matter (241); Stellar mass loss (1613)

1. Introduction

Interacting supernovae (SNe) are explosive transients showing observational signs of shock interaction between their ejecta and pre-existing circumstellar material (CSM; see, e.g., S. Blinnikov 2017; N. Smith 2017; M. Fraser 2020; L. Dessart 2024; A. Gangopadhyay 2024). Although a fraction of interacting SNe are thermonuclear explosions of white dwarfs within an H-rich CSM (Type Ia CSM SNe; M. Hamuy et al. 2003; B. Dilday et al. 2012; J. M. Silverman et al. 2013), in most cases they are core-collapse (CC) SNe embedded in H-rich (Type IIn; E. M. Schlegel 1990; A. V. Filippenko 1997) or He-rich/H-poor CSM (Type Ibn; A. Pastorello et al. 2008a). For an increasing number of observed SNe, strong evidence suggests that shock interaction seems a ubiquitous phenomenon in stripped envelope (SE) SNe (A. E. Niblett et al. 2025).

Type IIn SNe show narrow H lines characterized by FWHM velocities ranging from a few tens to a few hundreds kilometers per second (e.g., M. Kiewe et al. 2012; F. Taddia et al. 2013; I. Salmaso et al. 2025). The radiation produced in the shock interaction between the SN ejecta and the CSM is the main source of powering the luminosity of SNe IIn, and is responsible for the diversity observed in their spectrophotometric properties (e.g., T. J. Moriya et al. 2013; F. Taddia et al. 2013; A. Nyholm et al. 2020; D. Hiramatsu et al. 2024a; C. L. Ransome & V. A. Villar 2025). The observed variety suggests that SNe IIn are characterized by a wide range of CSM parameters (expansion velocity, geometry, density profile, distance from the progenitor) and, hence, different progenitor's mass-loss channels and pre-eruptions (T. J. Moriya et al. 2014). For instance, the multipeaked light curves of some SNe IIn[55] are likely caused by ejecta collisions with shell-like gas distributions, most likely produced through eruptive mass-loss events rather than steady winds.

The spectra of Type Ibn SNe show narrow lines of He I (with FWHM velocities ranging from hundreds to ∼1000–3000 km s^{-1}) but have little or no evidence of H (e.g., A. Pastorello et al. 2016; G. Hosseinzadeh et al. 2017), revealing the interaction of SN ejecta with He-rich CSM (N. Smith et al. 2008; N. Smith 2017; K. Maeda & T. J. Moriya 2022). SNe Ibn show a moderate heterogeneity in the photometric evolution (G. Hosseinzadeh et al. 2017). While a limited number of outliers is known,[56] most SNe Ibn have fast-evolving light curves, with a short rise time (⩽1 week), a rapid post-peak decline, and a high luminosity at maximum, reaching peak absolute magnitudes of $-20.0 \leqslant M_R \leqslant -18.5$ mag (e.g., A. Pastorello et al. 2016; G. Hosseinzadeh et al. 2017; Z. Y. Wang et al. 2024). Such events are generally considered as stripped envelope (SE) CC explosions of massive stars occurring in a He-rich CSM (e.g., A. Pastorello et al. 2007; T. J. Moriya & K. Maeda 2016; K. Maeda & T. J. Moriya 2022). However, in some cases, their observed parameters can be comfortably explained as the explosion of much lower-mass He stars in binary systems, whose H-rich envelope was stripped by the interaction with the companion star (e.g., N. E. Sanders et al. 2013; G. Hosseinzadeh et al. 2019; L. Dessart et al. 2022).

In the past decade, we discovered that a significant fraction of SNe IIn may explode a short time after major stellar outbursts (see, e.g., R. J. Foley et al. 2011; E. O. Ofek et al. 2013; A. Pastorello et al. 2013; N. L. Strotjohann et al. 2021; A. Reguitti et al. 2024). However, precursor outbursts were also detected from the inspection of archival images of SNe Ibn (e.g., SN 2023fyq; see S. J. Brennan et al. 2024; Y. Dong et al. 2024). This is an important step to improve our understanding of SNe Ibn, as studying eruptive mass-loss events from their progenitors allows us to probe the latest evolutionary stages of stripped massive stars before their explosion.

[55] E.g., iPTF13z (A. Nyholm et al. 2017), SNe 2005ip (M. Stritzinger et al. 2012), 2006jd (M. Stritzinger et al. 2012), 2009ip (A. Pastorello et al. 2013; M. Fraser et al. 2013), 2013gc (A. Reguitti et al. 2019), 2021qqp (D. Hiramatsu et al. 2024b), and 2023zkd (A. Gagliano et al. 2025).

[56] OGLE-2012-SN-006 (A. Pastorello et al. 2015a), iPTF13beo (E. Gorbikov et al. 2014), OGLE-2014-SN-131 (E. Karamehmetoglu et al. 2017).

2. Host Environment

The discovery of SN 2022pda[57] was announced by the Pan-STARRS Survey for Transients (M. D. Fulton et al. 2025) using the Panoramic Survey Telescope and Rapid Response System 2 (Pan-STARRS2—PS2; K. C. Chambers et al. 2016) on 2022 July 19 (MJD=59779.56), and later confirmed by the Asteroid Terrestrial-impact Last Alert System (ATLAS; J. L. Tonry et al. 2018a, 2018b; K. W. Smith et al. 2020) on 2022 August 23 (MJD 59814.22). The classification was performed by M. Fulton et al. (2022) on 2022 September 25 as a Type Ibn SN. Additionally, M. Fulton et al. (2022) noted pre-rise activity lasting 70 days before peak in the Pan-STARRS data. Its coordinates are $\alpha = 22^{h}04^{m}13^{s}.895$, $\delta = -18°49' 40''.46$ [J2000], and it is offset by $15''.6$ south and $10''.4$ west from the center of the likely host galaxy LEDA 135305. In the framework of a standard cosmology (H_0=73 km s^{-1} Mpc^{-1}, Ω_M=0.27, Ω_Λ=0.73), we adopted a kinematic distance d = 253.8 ± 17.8 Mpc (μ = 37.02 ± 0.15 mag) for the galaxy, which has been corrected for the influence of the Virgo cluster, the Great Attractor, and the Shapley supercluster (J. R. Mould et al. 2000). The Galactic reddening toward SN 2022pda is small, $E(B - V)_{\rm Gal}$ = 0.022 mag (E. F. Schlafly & D. P. Finkbeiner 2011), assuming a reddening law with $R_V = 3.1$ (J. A. Cardelli et al. 1989). To estimate the additional host galaxy reddening, we measured the equivalent width (EW) of the Na I D ($\lambda\lambda$5890,5896) absorption at the redshift of the host galaxy using the early, moderate-resolution SN spectrum taken with the Very Large Telescope (VLT)/X-Shooter. We obtain Na I D1 and D2 EWs of 0.33 and 0.25 Å, i.e., EW $({\rm D1+D2})_{\rm Host}$ = 0.58 Å. Following the Equation 9 in D. Poznanski et al. 2012 (i.e., $\log_{10}(E(B - V))$=1.17 × EW (D1+D2) − 1.85 ± 0.08), we obtain a host galaxy reddening of $E(B - V)_{\rm Host}$ = 0.07 mag. In order to be consistent with the recalibration of Milky Way extinction in E. F. Schlafly & D. P. Finkbeiner (2011), we further multiplied this value by the re-normalization factor of 0.86, resulting in $E(B - V)_{\rm Host}$ = 0.06 mag (see R. Dastidar et al. 2025; A. Gangopadhyay et al. 2025). Throughout this Letter, we thus adopt a total line-of-sight color excess of $E(B - V)_{\rm Total}$ = 0.08 mag.

3. Photometric Observations

The multiwavelength optical (Johnson–Cousins *UBV*, Sloan *ugriz*) and near-infrared (NIR; *JHK*) follow-up of SN 2022pda started soon after its classification, using the telescopes and the instruments listed in Table 1 (Appendix A.1). In addition to the ground-based observations, imaging in the ultraviolet (UV: UVW2, UVM2, UVW1) and optical (*UBV*) domains was obtained through the Neil Gehrels Swift Observatory (Swift) equipped with the Ultra-violet Optical Telescope (UVOT; e.g., P. W. A. Roming et al. 2005; T. S. Poole et al. 2008; A. A. Breeveld et al. 2010) in the UVW2, UVM2, UVW1, *U*, *B*, *V* bands (N. Gehrels et al. 2004). Simultaneously, Swift X-ray Telescope (XRT; D. N. Burrows et al. 2005) observed SN 2022pda on five occasions, starting on 2022 September 27. XRT collected a total exposure of 11.9 ks. SN 2022pda is not detected with a 3σ upper limit of 1.8×10^{-3} cts s^{-1} in the 0.3–10 keV energy band. Assuming a power-law spectrum with photon index $\Gamma = 2$ and the Galactic absorption (2.2×10^{20} cm^{-2}), this implies an upper limit on the 0.3–10 keV unabsorbed average flux of 4×10^{-14} erg s^{-1} cm^{-2}. At 253.8 Mpc, this translates to an X-ray luminosity $L_X < 4 \times 10^{41}$ erg s^{-1}. Considering instead only the first 3.7 ks observation taken a few days before the optical peak, the upper limit is 2.2 times higher.

Finally, one epoch of mid-infrared (MIR) photometry in the W1 (3.4 μm) and W2 (4.6 μm) filters was obtained with the Wide-field Infrared Survey Explorer (WISE) space telescope (E. L. Wright et al. 2010). The reduction techniques adopted for our photometric dataset are extensively discussed in Appendix A.2. Along with the observations obtained through our monitoring programs, photometric data are also provided by the major sky surveys: Zwicky Transient Facility (ZTF; E. C. Bellm et al. 2019; M. J. Graham et al. 2019), ATLAS (J. L. Tonry et al. 2018b; K. W. Smith et al. 2020) and Pan-STARRS (K. C. Chambers et al. 2016; M. D. Fulton et al. 2025). These survey data are important for tracking the progenitor star activity before the SN discovery. The final UV, optical, and infrared (IR) magnitudes are available at the CDS.

3.1. Light Curves

The multiband (UV-Optical-IR) light curves of SN 2022pda are shown in Figure 1. Two main photometric properties are immediately noticeable: (1) signs of photometric variability at the SN location are visible before the SN explosion; (2) the SN light curve clearly shows two humps in all bands.

The SN 2022pda site was sampled by the main surveys for ∼3 yr before its discovery. The earliest observation of the field is from Pan-STARRS, and is dated 2019 November 13 (MJD = 58800.222). At that time, the object was not detected down to an *i*-band limit of 21.5 mag. Then the field was occasionally monitored from 2019 November to 2022 June, but only upper limits were obtained. Although the Pan-STARRS discovery was announced on 2022 July 19 at i = 20.28 ± 0.12 mag, an earlier detection was obtained by ZTF on 2022 June 7 (MJD = 59737.436), with the source being at a magnitude g = 21.24 ± 0.32 mag. ATLAS confirmed the SN discovery on 2022 August 23, also providing an earlier detection on 2022 June 10 (MJD = 59740.599) at c = 20.36 ± 0.26 mag.

As shown in Figure 1, the ZTF, ATLAS, and Pan-STARRS light curves reveal a photometric variability lasting ∼100 days (from MJD = 59737 to MJD = 59839; with a luminosity rise of ∼2 mag) prior to major SN brightening. This 2 mag rise closely resembles those observed in SN 2009ip-like objects (the so-called "Event A"; see M. Fraser et al. 2013; A. Pastorello et al. 2013). Then, the light curve of SN 2022pda reached a local minimum on 2022 September 18 (MJD = 59840.3), which is tentatively assumed to be the SN explosion epoch. This minimum is followed by a rapid rise of the light curve (∼2 mag in about 2 weeks) that reached a first blue peak. The photometric parameters at the SN maximum light were obtained through low-order polynomial fits. The epoch of the *r*-band peak is estimated to be on MJD = 59856.7 ± 0.7, which will be used as a reference time throughout this Letter. The peak magnitude is $r_{\rm max}$ = 17.6 ± 0.1 mag. The light curve shows a fast linear decline after maximum in all bands, with decline rates of 6.61 ± 0.87, 4.42 ± 0.35, 2.84 ± 0.15, and 2.94 ± 0.55 mag per 100 days in the UVW2, *B*, *r*, and *z* filters, respectively. This initial rapid decline is then followed by a

[57] The object is also known with survey designations PS22gdx, ATLAS22bbxi, and ZTF22aawxlpc.

slower decline, and a sort of short-duration plateau is observed in the best-sampled red bands.

After this flattening, the multiband light curves decline again to a local minimum at ∼+60 days, followed by a new brightening. However, the monitoring campaign was suspended at ∼+95 days, as the SN was approaching solar conjunction. This late re-brightening likely indicates the onset of an enhanced ejecta–CSM interaction event. After the seasonal gap and the second peak, we obtained a few epochs of late photometric data while the SN magnitude was approaching the instrumental detection thresholds.

In Figure 2, we compare the $R/r-$ band absolute light curves (top-left panel), the $R-I/r-i$ color curves (top-right panel), the quasi-bolometric light curves (bottom-left panel), and the peak magnitude versus rise time parameters (bottom-right panel) of SN 2022pda with those of the transitional IIn/Ibn SNe 2005la, 2011hw, and 2021foa; the H-rich SNe 2009ip and 2013gc; the double-peaked, He-rich Type IIn SN 2023zkd, and a sample of Type Ibn SNe. The $R/r-$ band absolute light curve shows that SN 2022pda is characterized by a double-hump light curve, resembling those of the Type IIn SN 2013gc, SN 2023zkd, and some transitional IIn/Ibn SNe. Another remarkable feature in the light curve of SN 2022pda is its pre-SN variability, which is similar to those seen before some SNe IIn (e.g., SNe 2009ip, 2010mc, 2013gc, 2015bh, AT 2016jbu, and SN 2023zkd; see M. Fraser et al. 2013; E. O. Ofek et al. 2013; A. Pastorello et al. 2013, 2018; N. Elias-Rosa et al. 2016; A. Reguitti et al. 2019; S. J. Brennan et al. 2022; A. Gagliano et al. 2025), and, more rarely, in transitional SNe Ibn/IIn (e.g., SN 2021foa; A. Reguitti et al. 2022; D. Farias et al. 2024; A. Gangopadhyay et al. 2025) and in the SN Ibn SN 2023fyq (S. J. Brennan et al. 2024; Y. Dong et al. 2024). Furthermore, the peak absolute magnitude of all SNe in the comparison lies in the range −17 to −19 mag, while SN 2022pda (with $M_{\rm r}=-19.6\pm0.2$ mag) is the brightest event in the sample.

During the pre-SN phase, the $r-i$ color of SN 2022pda shows a modest increase from ∼0.2 mag at ∼−100 days to ∼0.3 mag at ∼−70 days, followed by a gradual blueward evolution to ∼0.2 mag at ∼−40 days and further to ∼0.1 mag at ∼−6 days (see the top-right panel of Figure 2). Around maximum light, the color remains relatively stable, fluctuating within ∼0.1–0.3 mag from −5 to +15 days without a clear monotonic trend. After this phase, the $r-i$ color begins an overall redward evolution, increasing from ∼0.2 mag to a peak of ∼0.5 mag at ∼+40 days. At later phases, the color becomes bluer again, decreasing to ∼0.3 mag by ∼+60 days, at a time coincident with the re-brightening seen in the light curve. SN 2021foa has a similar color evolution, but it is systematically bluer than SN 2022pda. The Type IIn SN 2009ip has a well-sampled pre-maximum color curve with a nearly flat color evolution ($r-i$∼0 mag), while its color becomes bluer again (∼−0.5 mag) at late times. SN 2006jc and SN 2011hw show a similar color evolution at phases <+ 70 days, both moving toward slightly redder colors. In particular, the ($r-i$) color of SN 2011hw reaches ≈ 0.7 mag at about +70 days. Later, the color of SN 2006jc increases rapidly from 0.8 mag (at +70 days) to 1.7 mag (at +130 days), which is likely associated with the formation of dust (E. Di Carlo et al. 2008; S. Mattila et al. 2008; G. C. Anupama et al. 2009). While the Type IIn SN 2013gc and SN 2023zkd do not have early observations, their $r-i$ colors show a modest evolution from −0.1 to 0.4 mag at phases later than +50 days. As expected, the comparison shows a large heterogeneity in the color evolution of interacting SNe.

We then computed a quasi-bolometric light curves for SN 2022pda and the comparison objects, following the prescriptions of Y.-Z. Cai et al. (2026). To proceed with a meaningful comparison between those transients, we constructed quasi-bolometric light curves integrating the fluxes in the optical bands, accounting for the distances and reddening estimates of each object. As shown in the bottom-left panel of Figure 2, SN 2022pda, SN 2011hw, and SN 2023zkd show a pronounced double-peak bolometric light curve. SN 2022pda with $L_{\rm SN\,2022pda}\sim2.1\times10^{43}$ erg s^{-1} is significantly more luminous than the other objects at peak. For reference, for four comparison objects, we determined the following values: $L_{\rm SN\,2011hw}\sim5.2\times10^{42}$ erg s^{-1}, $L_{\rm SN\,2009ip}{\sim}2.9\times10^{42}$ erg s^{-1}, $L_{\rm SN\,2005la}\sim1.1\times10^{42}$ erg s^{-1}, and $L_{\rm SN\,2023zkd}{\sim}6\times10^{42}$ erg s^{-1}).

Figure 2 (bottom-right panel) shows the peak absolute magnitude versus rise time diagram including SN 2022pda and other ejecta–CSM interacting comparison objects. This plot shows that SN 2022pda has an intermediate peak absolute magnitude ($M_{\rm r}\approx-19.6$ mag) in the context of the Type Ibn SN sample, whereas it lies in the slower tail (∼16 days) of the rise time distribution. We remark that transitional Type IIn/Ibn events have a wide range of observed peak absolute magnitudes ($-19.6\leqslant M_{\rm R/r}\leqslant-16.5$ mag), and in general longer rise times ($16\leqslant t\leqslant24$ days) than typical SNe Ibn ($t\leqslant10$ days).

4. Spectroscopic Observation

Following the classification of SN 2022pda, we launched a spectroscopic follow-up campaign using a number of facilities, during which we obtained 19 spectra spanning a period from about −10 days to +70 days relative to maximum light. Then, spectroscopic monitoring was suspended because the object approached the solar conjunction. Usually, the spectra were reduced following standard prescriptions, but in some cases we used dedicated pipelines. The data reduction steps and information on the spectra of SN 2022pda are detailed in Appendix A.3. The basic parameters of the instruments used are reported in Table 2. The resulting spectra of SN 2022pda are shown in Figure 3.

4.1. Spectral Evolution

The earliest spectrum shows a blue continuum with a blackbody temperature $T_{\rm BB}\geqslant$ 15,500 K [58] (at −9.3 days), along with narrow He and prominent Hα emission lines, suggesting that it is a transitional Type Ibn/IIn event. Four days later (at −5.6 days), we obtained a higher-resolution optical+NIR spectrum using VLT/X-Shooter. In this spectrum, emission lines of He I λλ3889, 4471, 4922, 5016, 5876, 6678, 7065, and 7281 are clearly detected, along with prominent Hα and Hβ. As highlighted in the middle panel of Figure 3, we identify numerous spectral features in the blue region (3800–5200 Å) of this spectrum. In particular, the broadest bump at 4600–4700 Å is tentatively identified as a blend of C III/N III/O II (M. Modjaz et al. 2009). Such lines can be interpreted as evidence of CNO-element enrichment in the progenitor's CSM. This suggests enhanced mixing from

[58] This value is considered a lower limit due to the lack of UV spectra, especially since the emission is UV-dominated during this early phase.

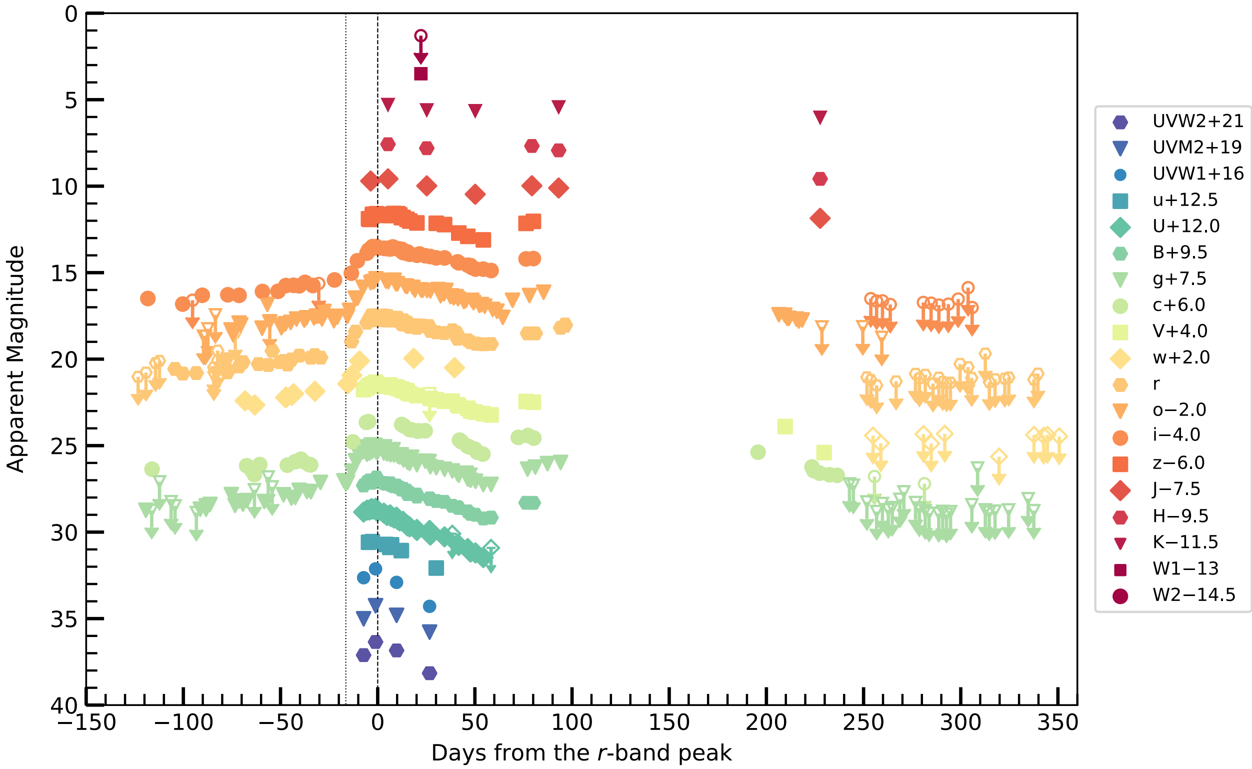

Figure 1. Multiband light curves of SN 2022pda. The dotted vertical line indicates the estimated explosion epoch, while the dashed vertical line marks the epoch of the r-band light-curve peak. Upper limits are marked with downward-pointing arrows. Each light curve is shifted by an arbitrary constant indicated in the legend for clarity. The error bars representing the uncertainties in the photometric data, in most cases, are smaller than the symbols. The phases are referred to the time of r_{max} (MJD = 59856.7).

the inner CNO burning regions to the outer layers. The He I λ5876 line has a clear P Cygni profile, with an intermediate-width Lorentzian emission component (with an FWHM velocity of about 3300 km s^{-1}) and a blueshifted Gaussian absorption. The position of the blueshifted absorption minimum indicates that the He-rich material is moving at a velocity of ∼1900 km s^{-1}. This line is likely produced in an unshocked CSM surrounding the SN. In the NIR spectrum (bottom panel of Figure 3), the most remarkable bump at 10,250–11,250 Å is possibly due to a blend of He I λ10830 and Paschen-γ λ10941 emission lines. We measured the position of the core of the blueshifted broad P Cygni absorption of He I λ10830, which is considered as a proxy for the velocity of the SN ejecta. Another shallow bump peaks near 18690 Å, which can be tentatively identified as He I λ18685–18697. However, there is no clear evidence that H (e.g., Paschen and Brackett series) lines can be securely identified in this NIR spectrum, likely because of the quite low signal-to-noise ratio (S/N).

From −5.6 days to +6.2 days, the spectra show a minor evolution in terms of feature strengths and line velocities. The H I and He I lines are still strong, and the pronounced bump visible in the 6400–6800 Å region is due to a blend of Hα and He I λ6678. The velocities derived from deblending the He I λ5876 line are ∼1900–2000 km s^{-1} from the wavelength of the P Cygni minimum, and ∼3300–4350 km s^{-1} from the FWHM of the Lorentzian emission component, similar to what was measured in the earlier spectra. The spectral continuum still remains quite blue with T_{BB} in the range 11,000–18,000 K. Subsequently, spectra at phases from +16.2 to +26.4 days show a redder continuum, with T_{BB} decreasing to 8700 ± 700 K (at +26.4 days). The line velocities increase with a broader emission component at v_{FWHM}≈ 4950 km s^{-1}. Hα and the He I λ6678 blend becomes more prominent, and now shows a clear "W"-shape profile. Another prominent feature is visible at 4600–5200 Å, likely a blend of Hβ, He I λ4922, and He I λ5016. In the last five spectra of SN 2022pda, obtained from +42.8 to +72.1 days, all of the emission features become more prominent. The velocity of the He I λ5876 line further increases, with a v_{FWHM}≈ 5800 km s^{-1} at +44.1 days and v_{FWHM}≈ 6700 km s^{-1} at +52.7 day. He I λ5876 with a narrow P Cygni profile is detected in the last spectrum (+72.1 days), with a velocity of about 2800 km s^{-1}, inferred from the position of the minimum of the P Cygni absorption relative to zero velocity position. In addition, we infer an FWHM velocity of the broadest component of the strong 6400–6800 Å bump of v_{FWHM} ≈ 12640 km s^{-1} in the +44.1 days spectrum, which decreases slightly to v_{FWHM} ≈ 10,230 km s^{-1} at +72.1 days.

It is worth noting that these late-time features have alternative plausible identifications. For instance, the bump at 4600–5200 Å can be a blend of Hβ, He I, and Fe II (multiplet 42), while the emission feature at about 5880 Å may also be due to the contribution of Na I D. Finally, the pronounced triple-peaked profile at 6400–6800 Å is likely due to high-velocity Hα components with a blue and a red emission bumps. The temperature of the continuum continued to decrease to a minimum T_{BB}=6620 ± 340 K at +52.7 days and subsequently increased to T_{BB}=7120 ± 100 K at +72.1 days. This late-time rise in temperature is consistent with the observed light-curve re-brightening.

In Figure 4, we compare the spectra of SN 2022pda obtained before maximum, around maximum, and at late times with the

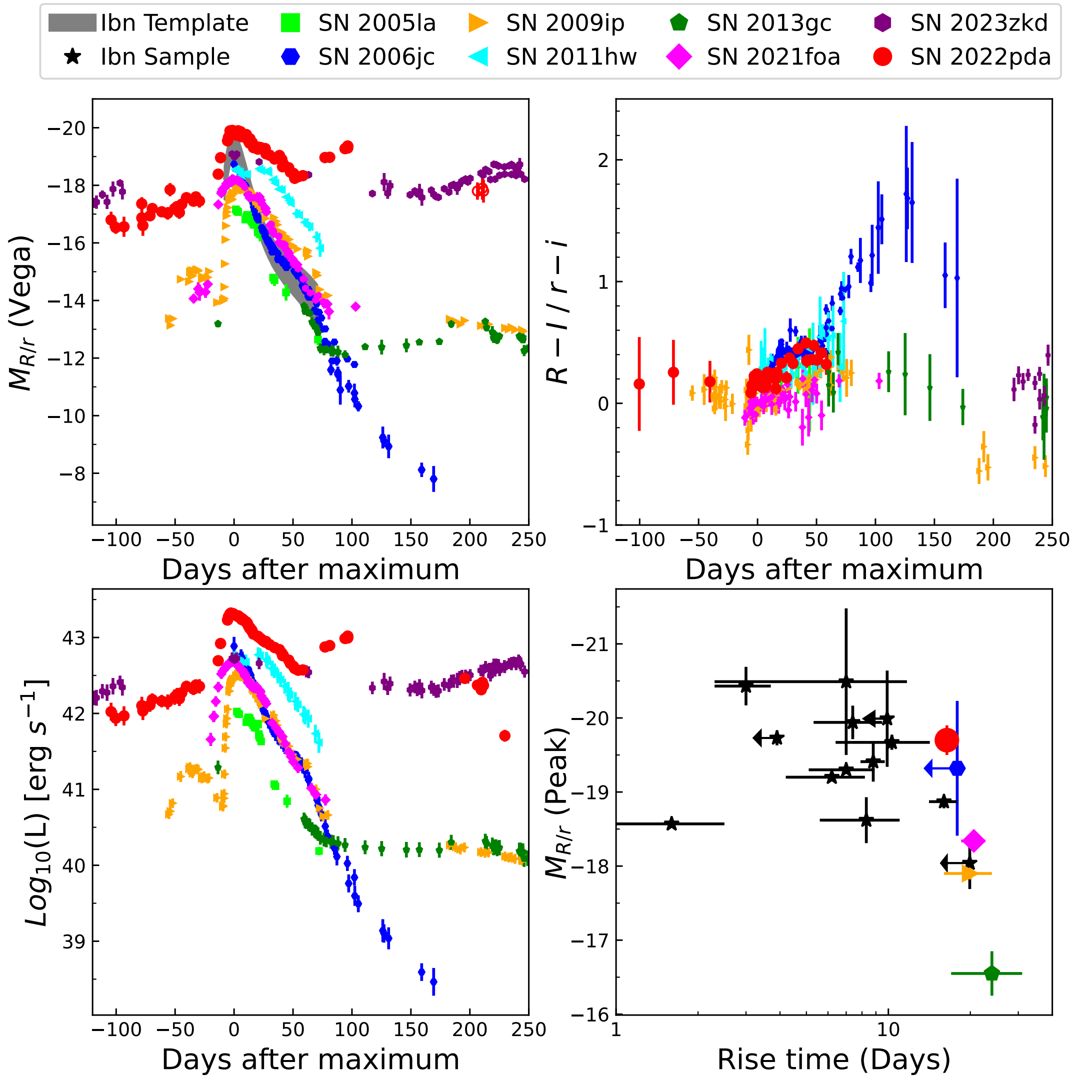

Figure 2. Comparisons of R / r-band light curves (top-left panel; after seasonal gap, the o-band data points are shown in empty circles for completeness.), $R-I$/ $r-i$ color (top-right panel), quasi-bolometric light curves (bottom-left panel), and peak magnitude versus rise time (bottom-right panel) of SN 2022pda with those of the transitional Type IIn/Ibn SNe 2005la, 2011hw, and 2021foa; the Type IIn SNe 2009ip and 2013gc; and a sample of SNe Ibn. The Type Ibn light-curve template is adopted from G. Hosseinzadeh et al. (2017). Data sources of comparison objects are from T. Matheson et al. (2000), R. J. Foley et al. (2007), A. Pastorello et al. (2007, 2008a, 2008b, 2013, 2015b, 2016), N. Smith et al. (2010, 2012a), M. Fraser et al. (2013), E. Gorbikov et al. (2014), I. Shivvers et al. (2016), S. J. Smartt et al. (2016), G. Hosseinzadeh et al. (2017), A. Reguitti et al. (2019), A. Reguitti et al. (2022), S.-Q. Wang & L. Li (2020), D. Farias et al. (2024), A. Gangopadhyay et al. (2025), and Z. Y. Wang et al. (2024).

prototypical Type Ibn SN 2006jc, the transitional Type IIn/Ibn SNe 2005la, 2011hw, and 2021foa, and the Type IIn SNe 2009ip, 2010jp, and 2013gc at similar phases. As shown in the left panel of Figure 4, all early spectra obtained before and around maximum light show a blue continuum with superposed narrow H and He lines. In this phase, SN 2022pda shows a blue continuum and narrow He I lines in the spectra, which are similar to those of other SNe Ibn (e.g., SN 2006jc). SN 2022pda and other transitioning SNe IIn/Ibn also display H lines, which are much weaker than in SN 2021foa and the H-rich SNe 2009ip and 2010jp. This comparison highlights the existence of a continuum in the spectral properties from SNe IIn to SNe Ibn, with SN 2022pda being a bridge connecting these two types. We note that the velocity of the He I λ5876 line (1900 km s^{-1}) in SN 2022pda is on the higher end, but still within the range of velocities measured in large samples of SNe Ibn at maximum light (see A. Pastorello et al. 2016; Z. Y. Wang et al. 2024).

Late-time ($\geqslant$30 days) spectra of SN 2022pda and the comparison objects show a major evolution. The continuum becomes redder, the H and He lines are now stronger and broader, while other lines (such as [O I] $\lambda\lambda$7774-7777 and λ8446) appear in the redder spectral region. In particular, the NIR Ca II triplet becomes clearly visible in SNe 2011hw, 2013gc, and 2006jc. We also note that the pronounced bump at 6400–6800 Å (tentatively identified as a triple-peaked Hα in SN 2022pda) shows a striking similarity with the Hα profile of SN 2010jp. SN 2010jp displays an unprecedented triple-peaked Hα line profile, characterized by a narrow central component (FWHM velocity $\geqslant$800 km s^{-1}), two bumps centered at $-$13,000 km s^{-1} (blue emission) and +15,000 km s^{-1} (red emission), and very broad wings extending from $-$22,000 to +25,000 km s^{-1} (see Figure 7 in N. Smith et al. 2012b). This feature was interpreted by N. Smith et al. (2012b) as a bipolar jet-driven explosion, where the central peak arises from ejecta–CSM interaction at mid and low latitudes, and the high-velocity components originate from a nonrelativistic bipolar jet. As shown in Figure 4 (right panel), the +72.1 days spectrum of SN 2022pda shows a similar Hα profile but with lower velocities for the two bumps centered at -5250 km s^{-1} and $+4000$ km s^{-1}, and broad wings extending from $-14{,}000$ to $+13000$ km s^{-1}. However, the narrow central component of SN 2022pda exhibits a relatively higher velocity than that of SN 2010jp, with an FWHM velocity of $\sim$3650 km s^{-1}.

The right panels of Figure 4 shows in detail the evolution of the Hβ (and He I λ4922, 5016; top) and Hα (and He I λ6678; bottom) line profiles of SN 2022pda in the velocity space. The Hα line shows an asymmetric shape with a two-component profile: a narrow absorption component at about -4000 km s^{-1} plus an emission feature at about -5000 km s^{-1}. As shown in the top-right panel of Figure 4, the Hβ profile and its evolution are similar to those of Hα.

5. Discussion and Conclusion

5.1. Pre-SN Activity

SN 2022pda shows a remarkable light curve with a moderately long ($\sim$100 days) pre-SN activity and two dominant post-explosion peaks.

A light-curve flattening is visible between 2022 October 29 (MJD = 59881) and November 8 (MJD = 59891), with a midpoint at MJD = 59886, hence approximately 46 days after the explosion. In analogy with similar features observed in other interacting SNe (e.g., SNe 2009ip, 2013gc, 2018cnf; see J. C. Martin et al. 2015; A. Pastorello et al. 2019; A. Reguitti et al. 2019), this short-duration plateau of SN 2022pda is likely produced by enhanced shock interaction between the SN ejecta and material expelled during a pre-SN outburst. Adopting a velocity of 4900 km s^{-1} for the SN ejecta (as estimated from the position of the minimum of the broad P Cygni profile of He I λ10830; see Section 4.1), they reach the innermost He-rich CSM layers at a distance of about 1.9×10^{15} cm. Assuming the He-rich CSM velocity is about 1900 km s^{-1} (see Section 4.1), this material was possibly ejected at about 0.32 yr ($\sim$119 days) before the explosion, which is roughly in agreement with the timescales of the observed pre-SN eruptive phase. We remark that similar eruptive phases have been observed in other interaction-powered SNe (e.g., N. L. Strotjohann et al. 2021, and references therein), and were tentatively explained as being due to binary interaction (N. Smith 2014; L. Dessart et al. 2022; B. D. Metzger 2022; D. Tsuna et al. 2024).

5.2. Light-curve Modeling

The persistent H and He emission lines and the light-curve morphology suggest that there is a significant contribution to the SN luminosity from the interaction between the SN ejecta and a dense CSM. Following this motivation, we model the bolometric light curve of SN 2022pda derived from blackbody fits to the broadband photometry, assuming that the radiation is fully powered by ejecta–CSM interaction.

We first discuss the effect of extended shock breakout inside CSM. As noted extensively in the previous literature, the large optical thickness of dense CSM can give rise to longer shock breakout phase (see, e.g., R. A. Chevalier & C. M. Irwin 2011; S. Ginzburg & S. Balberg 2012, as well as R. Chiba & T. J. Moriya 2024 for double-peaked interacting SNe in particular) than typical CC SNe. However, as pointed out in R. Chiba & T. J. Moriya (2024), it is difficult to reconcile double-peaked light curves with this interpretation when (1) the second peak is comparably bright to the first peak and (2) the separation between the peaks is longer than the rise time of the first peak. This is because the density requirement for a bright second peak is in conflict with the relatively rapid rise from the breakout. Since the light curve in Figure 2 satisfies both of the conditions, we consider the scenario where the shock breakout dominates the first peak to be unlikely.

To reconstruct the CSM density profile, we follow the approach of D. Hiramatsu et al. (2024b), which is based on the formalism of T. J. Moriya et al. (2013) that derives the contribution of the interaction to the luminosity under the approximation of a thin shell for the emitting region (also see, e.g., R. A. Chevalier 1982; R. A. Chevalier & C. Fransson 1994; C. D. Matzner & C. F. McKee 1999; G. Svirski et al. 2012). This method has been used to interpret the light curves of SN 2021qqp (D. Hiramatsu et al. 2024b) and SN 2023zkd (A. Gagliano et al. 2025), both interacting SNe with double-peaked light curves and precursor detections.

We assume that the ejecta follows a broken power-law density profile with $\delta = 0$, $n = 10$ (corresponding to the explosion of stars with radiative envelopes; C. D. Matzner & C. F. McKee 1999). The radiative efficiency ε is set to a constant value of $\varepsilon = 0.3$ for both the forward and reverse shocks, in line with the observation of interacting SNe (e.g., C. Fransson et al. 2014). Based on the analysis of the He emission lines in Section 4.1, we set the CSM velocity to 1900 km s^{-1}. We assume that the interaction started 0.1 day after the explosion, and the initial shell velocity is assumed to be 10,000 km s^{-1}, in line with A. Gagliano et al. (2025).

We consider different combinations of ejecta masses and explosion energies: ($M_{\rm ej}$, $E_{\rm ej}$)=(5 $M_\odot$, 5 B);(5 $M_\odot$, 10 B); (10 $M_\odot$, 5 B); and (10 $M_\odot$, 10 B). The evolution of the shell velocity in each model is shown in the left panel of Figure 5, while the reconstructed CSM density profile for each combination of explosion parameters is shown in the middle panel of Figure 5. The total CSM masses in each model are 13.5 $M_\odot$, 8.0 $M_\odot$, 21.3 $M_\odot$, and 5.5 $M_\odot$, respectively. As noted in D. Hiramatsu et al. (2024b), higher masses of CSM are required for lower explosion energies, in order to extract a larger fraction of kinetic energy from the ejecta. Heavier CSM mass is required for SN 2022pda than similar, less-luminous objects in literature: 2.7 $M_\odot$ for (10 $M_\odot$, 4 B) in SN 2021qqp (D. Hiramatsu et al. 2024b), 5–6 $M_\odot$ for (10 $M_\odot$, 2 B) in SN 2023zrk (A. Gagliano et al. 2025).

We can convert the CSM density profile into pre-explosion mass-loss rate through an assumption of the CSM expansion velocity. Assuming a constant $v_{\rm CSM}$ = 1900 km s^{-1}, the resulting evolution of the mass-loss rate is shown in the right panel of Figure 5. In order to power the double-peaked light curve of SN 2022pda, two separate mass-loss events are required: both of them with a mass-loss rate of $\sim 5 M_\odot {\rm yr}^{-1}$, but that occurred $\sim$0.2 yr (roughly consistent with the detected pre-SN activity; see discussion in Section 5.1) and $\sim$1 yr before the explosion, respectively.

Finally, we discuss the effect of CSM optical thickness. As pointed out in D. Hiramatsu et al. (2024b), it is not entirely trivial whether we should expect CSM to be optically thick or thin in this interpretation. On one hand, a denser CSM is favorable in order for the reprocessing of dissipated kinetic energy to radiation to be effective. On the other hand, in order

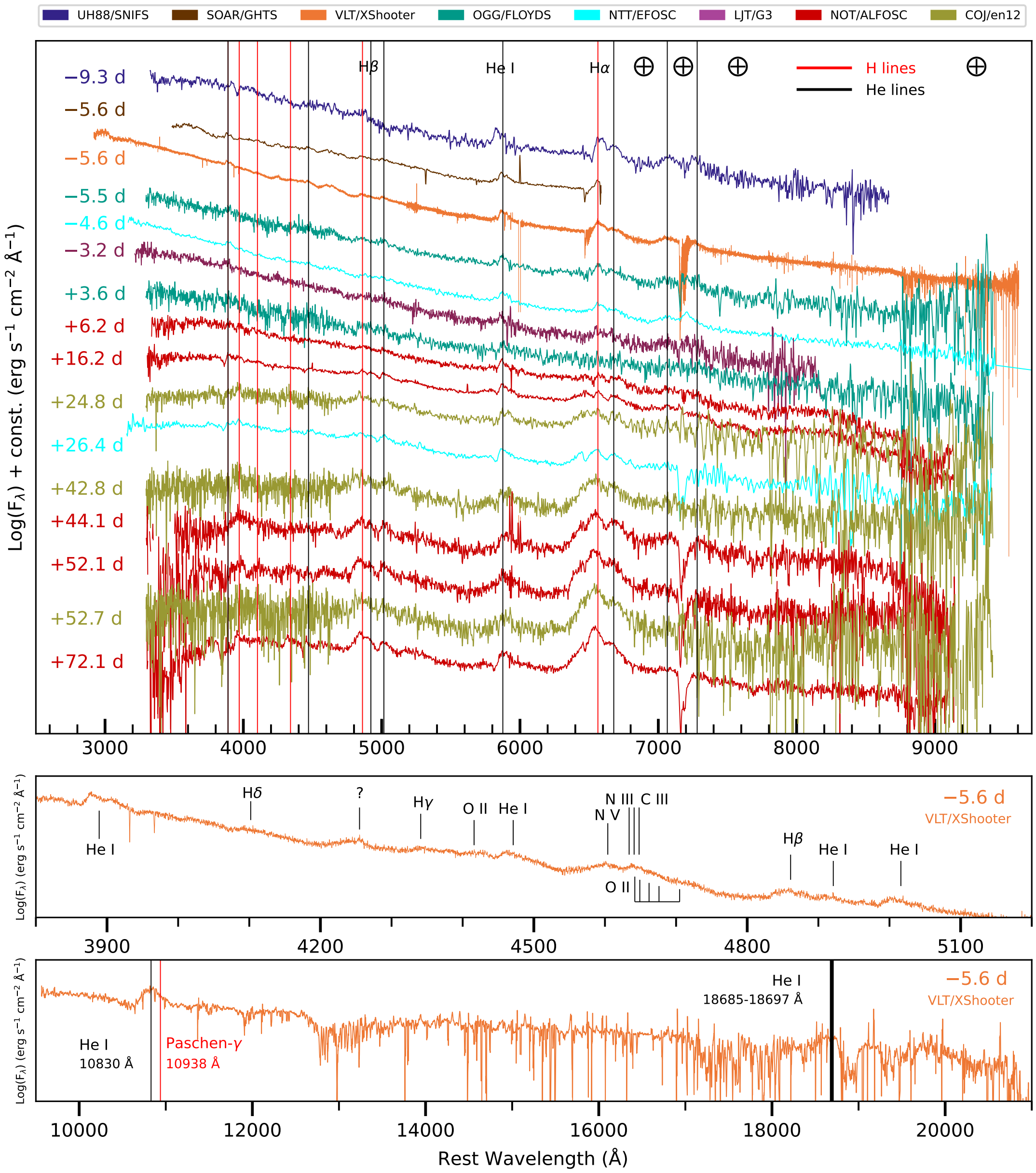

Figure 3. Spectroscopic evolution of SN 2022pda. Top panel: sequence of optical spectra between phases −9.3 days and +72 days. Vertical lines mark the positions of the most prominent Balmer and He I lines. Middle panel: identification of the most prominent lines in the blue part (3800–5200 Å) of the Very Large Telescope (VLT)/X-Shooter spectrum obtained on 2022 September 29. Bottom panel: identification on the −5.6 day VLT/X-Shooter NIR spectrum. This spectrum has been binned to 20 Å to increase the signal-to-noise ratio (S/N). Reddening and redshift corrections have been applied in all spectra. The positions of most significant telluric bands are marked with the symbol '⊕'. Some lower S/N spectra are not shown in this figure, while they are listed in the Table 2 (Appendix A.3).

to sustain a longer interaction-powered phase, CSM should be less dense for the shock breakout to occur earlier. The more detailed modeling incorporating the effects of diffusion inside CSM and asphericity is deferred to future works.

5.3. Spectroscopic Implication

In general, the spectroscopic evolution of SN 2022pda is similar to that of typical SNe Ibn in the shape of pseudo-continuum, the line identification, the line profiles, and velocities (see details in Section 4). However, the main difference between normal SNe Ibn and SN 2022pda is the existence of prominent H emission lines. This feature suggests that SN 2022pda is a new case of transitioning SN Ibn/IIn, occasionally observed in the past (e.g., SNe 2005la, 2011hw, 2021foa; see A. Pastorello et al. 2008b; N. Smith et al. 2012a; A. Pastorello et al. 2015b; A. Reguitti et al. 2022; D. Farias et al. 2024; A. Gangopadhyay et al. 2025). However, the discovery of these transitional interacting SNe suggests a continuum in the properties between at least some SNe IIn and SNe Ibn. The intensity of the H lines gradually decreases from the H-dominated SNe IIn, through SN 2009ip-like (with strong H plus weak He), SN 2021foa (with strong H and He), to SNe Ibn (only showing narrow He I), with SN 2022pda sitting somewhere between them. In this context, SN 2022pda and other SN Ibn/IIn events are proposed to result from the explosion of massive stars that were transiting from the luminous blue variable (LBV) to the Wolf–Rayet (W-R) stages (see Section 5.4, and A. Pastorello et al. 2008b, 2015b; N. Smith et al. 2012a; A. Reguitti et al. 2022). As a further

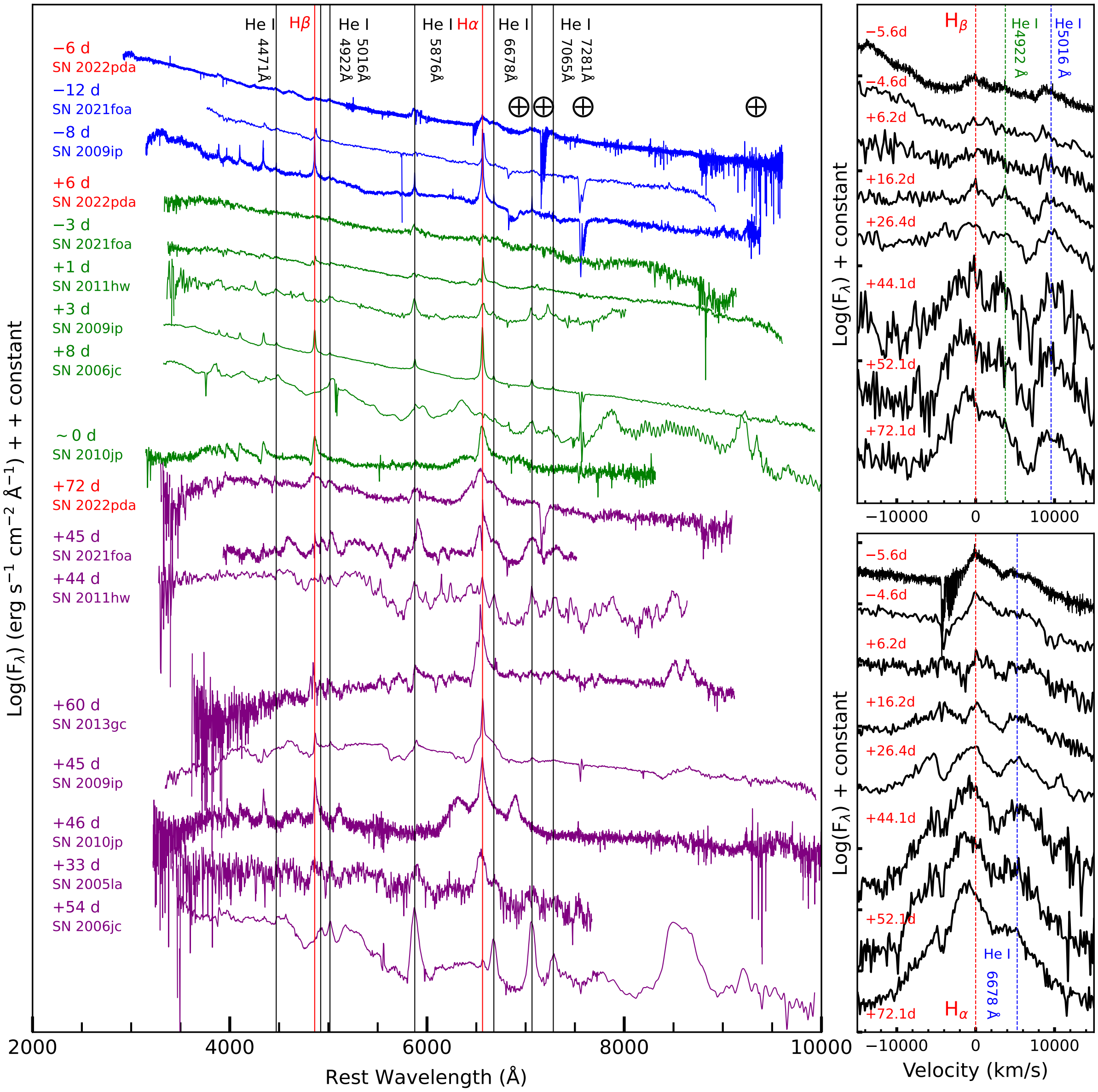

Figure 4. Left panel: comparison of SN 2022pda spectra with those of reference objects at similar phases: before the light-curve peak (blue), around maximum (green), and at late times (purple). The most relevant lines (Hα , Hβ , and the main He I lines) are marked with vertical lines. The '⊕' symbols mark the principal telluric absorption. Right panel: close up of the regions of Hα and Hβ of SN 2022pda spectra in velocity space. Hα , Hβ , and He I lines are highlighted by vertical lines.

support, the CSM velocity (1900 km s^{-1}) measured for SN 2022pda is consistent with that expected in W-R winds (of the order of 10^3km s^{-1}), which is significantly faster than LBV winds (N. Smith 2017).

The broad spectral bumps at 4600–5200 Å, 6400–6800 Å regions in the spectra SN 2022pda reveal a complex profile. This can be attributed to blends of H, He, and other emission lines, or to only H features coming from multiple emitting regions. We note that H spectral lines with a triple-peak profile, similar to that observed in SN 2022pda spectra, were observed in the Type IIn SN 2010jp. For that object, N. Smith et al. (2012b) proposed a possible jet-like ejection of H-rich material. In this context, SN 2022pda may have a similar asymmetric geometry as SN 2010jp, with the CSM having a more He-rich composition.

When the spectral lines of an interacting SN exhibit a composite profile, a plausible explanation is offered by invoking the interaction of the SN ejecta with an asymmetric CSM (for instance, with a disk-like structure or a torus). This scenario has been proposed for interacting transients showing two-humped light curves (see Y. Dong et al. 2024; D. Hiramatsu et al. 2024b; A. Gagliano et al. 2025; A. Gangopadhyay et al. 2025). In the case of SN 2022pda, a disk-like CSM formed through previous mass-loss events. Hence, the first SN light-curve peak is driven by the strong interaction between the SN ejecta and the surrounding CSM in the equatorial region. After that, the second major interaction event occurred, but with a longer duration than the first one. This is likely due to the collision of the ejecta with a more expanded, lower-density CSM.

5.4. Progenitor Scenarios

The general consensus on the origin of SNe Ibn is the terminal explosion of massive, H-poor W-R stars within He-rich CSM (e.g., R. J. Foley et al. 2007; A. Pastorello et al. 2007;

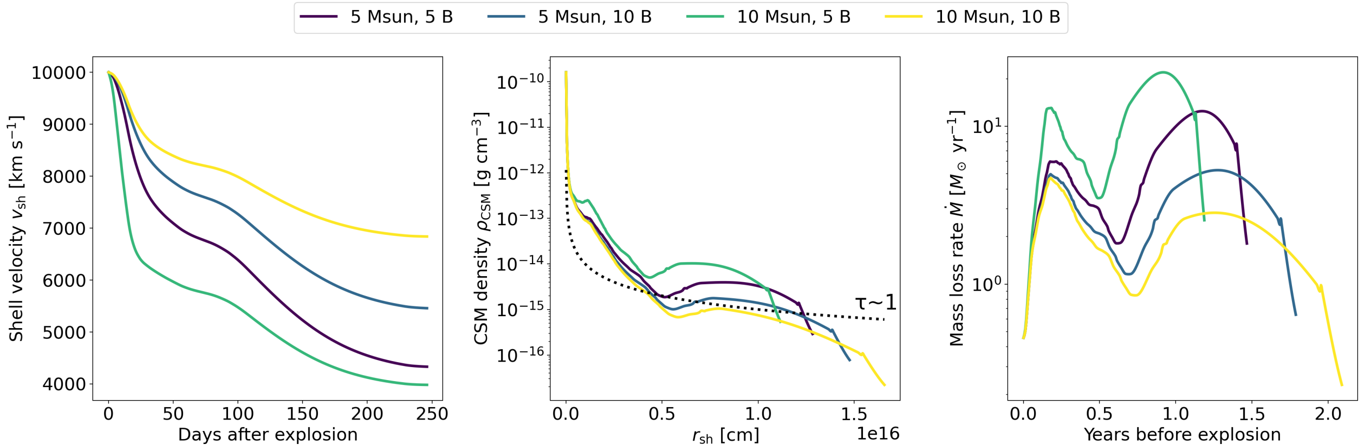

Figure 5. CSM interaction models with different assumptions for ejecta masses and explosion energies. Left panel: evolution of the shell velocity. Middle panel: CSM density distribution reconstructed from bolometric light curve of SN 2022pda for different ejecta masses and explosion energies. The dotted line shows the rough estimate of CSM optical depth, $\rho = 1/(\kappa r_{\rm sh})$ with a fiducial value of $\kappa = 0.1$ cm^2 g^{-1} representing the scattering opacity of ionized H-poor CSM. Right panel: evolution of pre-explosion mass-loss rate under the assumption of constant CSM expansion velocity $v_{\rm CSM} = 1900$ km s^{-1}.

N. Tominaga et al. 2008; K. Maeda & T. J. Moriya 2022), while LBVs are possible progenitors for SNe IIn and SN 2009ip-like events (e.g., N. Smith et al. 2010; R. J. Foley et al. 2011; J. C. Mauerhan et al. 2013; L. Dessart et al. 2015; J. De La Rosa et al. 2017; I. Boian & J. H. Groh 2019; C. L. Ransome & V. A. Villar 2025). However, recent results suggest that they may have lower-mass origins in interacting binaries (see, e.g., J. P. Anderson et al. 2012; H. Kuncarayakti et al. 2018; N.-C. Sun et al. 2020; L. Dessart et al. 2022; Z. Niu et al. 2026). SN 2022pda has somewhat hybrid properties between SNe Ibn and IIn, based on the observed photometric and spectroscopic properties, along with the light-curve modeling. Our findings suggest that the progenitor of SN 2022pda was a late-type W-R star with hydrogen (WNH), or even an Ofpe/WN9 (P. S. Conti 1975; N. R. Walborn 1977, 1982; L. Bianchi et al. 2004). However, precursor activity and a highly asymmetric CSM distribution (disk-like or bipolar) are comfortably the outcomes of binary interactions, without necessarily invoking massive W-R progenitors (e.g., N.-C. Sun et al. 2020; L. Dessart et al. 2022; D. Tsuna et al. 2024).

5.5. Concluding Remarks

In this letter, we presented new data and the analysis of the photometric and spectroscopic properties of the interacting SN 2022pda, which shows transitional features between those of a Type Ibn and a Type IIn SN. SN 2022pda reveals the existence of a continuum in the properties, such as progenitor types (from W-Rs to LBVs), mass-loss mechanisms, CSM configuration, from SNe Ibn to SN IIn. The upcoming operation of 10 yr Legacy Survey of Space and Time (LSST; Ž. Ivezić et al. 2019) at the Vera C. Rubin Observatory[59] will discover a large sample of transitional objects and reveal in detail the pre-SN photometric variability of SNe Ibn. Next-generation instruments such as the Chinese Space Station Telescope[60] will be helpful for studying the progenitors of these and new species of ejecta–CSM interacting transients (M. Fraser et al. 2021; S. Schulze et al. 2025). Advanced models are required to accurately interpret the photometric and spectroscopic data, and to establish a clear picture of the nature of SN 2022pda-like transients.

[59] https://www.lsst.org/
[60] http://nao.cas.cn/csst/

Acknowledgments

We thank the anonymous referee for providing insightful comments and suggestions that improved the Letter. This work is supported by the B-type Strategic Priority Program of the Chinese Academy of Sciences (grant No. XDB1160202), the National Key R&D Program of China with grants 2021YFA1600404 and 2024YFA1611603, the National Natural Science Foundation of China (NSFC grants 12303054, 12173082, 12333008, 12288102, 12033003, and 11633002), the Yunnan Fundamental Research Projects (YFRP; grants 202401AU070063, 202501AV070012, 202501AS070078, and 202401BC070007), the Top-notch Young Talents Program of Yunnan Province, the Light of West China Program provided by the Chinese Academy of Sciences, and the International Centre of Supernovae (ICESUN), Yunnan Key Laboratory of Supernova Research (No. 202505AV340004). Y.-Z. Cai, A.R., G.V., and I.S. acknowledge financial support from the SOXS project (PI S. Campana). S.C. acknowledges funding from the Italian Space Agency (ASI/INAF Contract I/004/11/6. We thank M. Fulton, A. Gkini, S. C. Williams, and M.-X. Huang for their assistance with observations and for sharing their data. A.P., A.R., E.C., G.V., N.E.R., I.S., S.B., and L.T. acknowledge support from the PRIN-INAF 2022, "Shedding light on the nature of gap transients: from the observations to the models." A.R. also acknowledges financial support from the GRAWITA Large Program grant (PI P. D'Avanzo). M.F. acknowledges financial support of Taighde Éireann—Research Ireland under grant No. 24/FFP-P/12959. T.E.M.B. is funded by Horizon Europe ERC grant No. 101125877. T.K. acknowledges support from the Research Council of Finland project 360274. T.-W.C. acknowledges the Yushan Fellow Program by the Ministry of Education, Taiwan for the financial support (MOE-111-YSFMS-0008-001-P1). S.J.B. acknowledge their support by the European Research Council (ERC) under the European Union's Horizon Europe research and innovation program (grant agreement No. 10104229—TransPIre). J.D. and R.P.S. acknowledge support by FCT for CENTRA through grant No. UID/PRR/00099/2025 (https://doi.org/10.54499/UID/PRR/00099/2025) and grant No. UID/00099/2025 (https://doi.org/10.54499/UID/00099/2025). J.D. acknowledges support by FCT under the PhD grant 2023.01333.BD, with DOI https://doi.org/10.54499/2023.01333.BD. R.P.S. acknowledges support by FCT under the PhD grant 2024.03599.BD. L.G. acknowledges financial support from AGAUR, CSIC, MCIN, and AEI 10.13039/501100011033 under projects PID2023-151307NB-I00, PIE 20215AT016, CEX2020-001058-M, ILINK23001, COOPB2304, and 2021-SGR-01270. M.D. Stritzinger acknowledges support from the Independent Research Fund Denmark (IRFD; grant 10.46540/2032-00022B). T.P. acknowledges the financial support from the Slovenian Research Agency (grants I0-0033, P1-0031, J1-8136, J1-2460, and Z1-1853). S.Mo. is funded by Leverhulme Trust grant RPG-2023-240. S.Z. is supported by the National Natural Science Foundation of China (NSFC, grant No. 12473031), the Yunnan Fundamental Research Projects (grant No. 202501AS070078) X.F.W. is also supported by the Tencent Xplorer Prize. S.J.S. and K.W.S. acknowledge funding from STFC grants ST/Y001605/1 and ST/X001253/1, a Royal Society Research Professorship and the Hintze Family Charitable Foundation. This work was funded by ANID, Millennium Science Initiative, ICN12_009.

We acknowledge the support of the staffs of the various observatories at which data were obtained. Based on observations collected at the European Organisation for Astronomical Research in the Southern Hemisphere, Chile, as part of ePESSTO+ (the advanced Public ESO Spectroscopic Survey for Transient Objects Survey—PI: Inserra). ePESSTO+ observations were obtained under ESO program IDs 108.220C and 111.24PR. Based on observations made with the Nordic Optical Telescope, owned in collaboration by the University of Turku and Aarhus University, and operated jointly by Aarhus University, the University of Turku, and the University of Oslo, representing Denmark, Finland, and Norway, the University of Iceland, and Stockholm University at the Observatorio del Roque de los Muchachos, La Palma, Spain, of the Instituto de Astrofisica de Canarias. Observations from the NOT were obtained through the NUTS2 collaboration which is supported in part by the Instrument Centre for Danish Astrophysics (IDA), and the Finnish Centre for Astronomy with ESO (FINCA) via Academy of Finland grant No. 306531. The data presented here were obtained in part with ALFOSC, which is provided by the Instituto de Astrofisica de Andalucia (IAA) under a joint agreement with the University of Copenhagen and NOTSA. The Liverpool Telescope is operated on the island of La Palma by Liverpool John Moores University in the Spanish Observatorio del Roque de los Muchachos of the Instituto de Astrofisica de Canarias with financial support from the UK Science and Technology Facilities Council. Funding for the LJT has been provided by Chinese Academy of Sciences and the People's Government of Yunnan Province. The LJT is jointly operated and administrated by Yunnan Observatories and Center for Astronomical Mega-Science, CAS. Based on observations collected at Schmidt telescope (Asiago Mount Ekar, Italy) of the INAF—Osservatorio Astronomico di Padova. This work makes use of data from the Las Cumbres Observatory Network and the Global Supernova Project. The LCO team is supported by U.S. NSF grants AST-1911225 and AST-1911151. We acknowledge the use of public data from the ATLAS, Pan-STARRS, ZTF, Swift, and WISE data archive.

Y.-Z. Cai: This paper is dedicated to the memory of my grandfather, a centenarian who lived to the age of 103. It is a poignant coincidence that this paper was accepted on the same day he was laid to rest.

Facilities: Swift (UVOT), Swift (XRT), WISE, TRAPPIST, Asiago:Schmidt, LCOGT, LT (IO:O), YAO:2.4m (YFOSC), NOT (ALFOSC), NOT (NOTCam), NTT (EFOSC2), NTT (SOFI), UH:2.2m (SNIFS), SOAR (GHTS), VLT (X-Shooter), FTN (FLOYDS), FTS (en12).

Software: astropy (Astropy Collaboration et al. 2013, 2018), Matplotlib (J. D. Hunter 2007), Numpy (C. R. Harris et al. 2020), SciPy (P. Virtanen et al. 2020), HEASoft (Nasa High Energy Astrophysics Science Archive Research Center Heasarc), HOTPANTS (A. Becker 2015), PESSTO pipeline (S. J. Smartt et al. 2015), SNIFS pipeline (M. A. Tucker et al. 2022), FLOYDS pipeline (S. Valenti et al. 2014), SExtractor (E. Bertin & S. Arnouts 1996).

Appendix
Ancillary Information for Photometric and Spectroscopic Data

A.1. Instrumental Setups

Table 1 lists the instrumental setups employed for the photometric observations of SN 2022pda, and Table 2 provides the log of its spectroscopic observations.

Table 1
Log of photometric observations of SN 2022pda

Code	Diameter (m)	Telescope	Instrument	Site
TRAPPIST	0.60	TRAPPIST-S Telescope	FLI ProLine	ESO La Silla Observatory, La Silla, Chile
Moravian	0.67/0.92	Schmidt Telescope	Moravian	Osservatorio Astronomico di Asiago, Asiago, Italy
fa01[a]	1.00	LCO (CPT site)	Sinistro	LCO node at South African Astronomical Observatory, Sutherland, South Africa
fa03[a]	1.00	LCO (LSC site)	Sinistro	LCO node at Cerro Tololo Inter-American Observatory, Cerro Tololo, Chile
fa04[a]	1.00	LCO (LSC site)	Sinistro	LCO node at Cerro Tololo Inter-American Observatory, Cerro Tololo, Chile
fa05[a]	1.00	LCO (ELP site)	Sinistro	LCO node at McDonald Observatory, Texas, USA
fa06[a]	1.00	LCO (CPT site)	Sinistro	LCO node at South African Astronomical Observatory, Sutherland, South Africa
fa07[a]	1.00	LCO (ELP site)	Sinistro	LCO node at McDonald Observatory, Texas, USA
fa11[a]	1.00	LCO (TFN site)	Sinistro	LCO node at Teide Observatory, Tenerife, Spain
fa12[a]	1.00	LCO (COJ site)	Sinistro	LCO node at Siding Spring Observatory, New South Wales, Australia
fa15[a]	1.00	LCO (LSC site)	Sinistro	LCO node at Cerro Tololo Inter-American Observatory, Cerro Tololo, Chile
fa16[a]	1.00	LCO (ELP site)	Sinistro	LCO node at McDonald Observatory, Texas, USA
fa19[a]	1.00	LCO (COJ site)	Sinistro	LCO node at Siding Spring Observatory, New South Wales, Australia
fa20[a]	1.00	LCO (TFN site)	Sinistro	LCO node at Teide Observatory, Tenerife, Spain
IO:O	2.00	Liverpool Telescope (LT)	IO:O	Observatorio Roque de Los Muchachos, La Palma, Spain
LJT	2.40	Lijiang 2.4 m Telescope	YFOSC	Gaomeigu site, Lijiang Observatory (LJO), Yunnan, China
ALFOSC	2.56	Nordic Optical Telescope (NOT)	ALFOSC	Observatorio Roque de Los Muchachos, La Palma, Spain
NOTCam	2.56	Nordic Optical Telescope	NOTCam	Observatorio Roque de Los Muchachos, La Palma, Spain
EFOSC2	3.58	New Technology Telescope (NTT)	EFOSC2	ESO La Silla Observatory, La Silla, Chile
SOFI	3.58	New Technology Telescope	SOFI	ESO La Silla Observatory, La Silla, Chile

Note.
[a] These telescopes are distributed globally at different observatory sites and form a network of Las Cumbres Observatory (LCO; T. M. Brown et al. 2013). These photometric data come from the Global Supernova Project (GSP) and the ePESSTO+/LCO time, while the spectroscopic data are all from GSP.

Table 2
Log of Spectroscopic Observations of SN 2022pda

Date	MJD	Phase[a] (days)	Telescope+Instrument	Grism/Grating+Slit	Spectral Range (Å)	Resolution (Å)	Exp. Time (s)
20220925	59847.4	−9.3	UH88+SNIFS	B/R+?	3400–9100	$R = 1000$	2700
20220929	59851.1	−5.6	SOAR+GHTS_RED	400_M1+1″0	3700–7000	6	1800
20220929	59851.1	−5.6	VLT+X-Shooter	UVB/VIS/NIR+1″0	3100–24,800	$R = 5400/8900/5600$	2 × 1550/2 × 1500/2 × 300
20220929	59851.2	−5.5	OGG 2m+FLOYDS	red/blu+2″0	3500–10,000	13	2699
20220930	59852.1	−4.6	NTT+EFOSC	gr11/gr16+1″0	3370–10,010	14	2400/2400
20221001	59853.5	−3.2	LJT+YFOSC	grism3+2″5	3500–8760	26	2100
20221008	59860.3	+3.6	OGG 2m+FLOYDS	red/blu+2″0	3500–10,000	13	2700
20221010	59862.9	+6.2	NOT+ALFOSC	gm4+1″0	3540–9700	14	2400
20221020	59872.9	+16.2	NOT+ALFOSC	gm4+1″0	3510–9700	14	3000
20221027	59879.4	+22.7	COJ 2m+en12	red/blu+2″0	3500–10,000	13	3600
20221029	59881.5	+24.8	COJ 2m+en12	red/blu+2″0	3500–10,000	13	3600
20221031	59883.1	+26.4	NTT+EFOSC	gr11/gr16+1″5	3350–9990	21	2 × 2100/2 × 2100
20221104	59887.4	+30.7	COJ 2m+en12	red/blu+2″0	3500–10,000	13	3600
20221110	59893.5	+36.8	COJ 2m+en12	red/blu+2″0	3500–10,000	13	3600
20221116	59899.5	+42.8	COJ 2m+en12	red/blu+2″0	3500–10,000	13	3600
20221117	59900.8	+44.1	NOT+ALFOSC	gm4+1″3	3720–9640	17	3000
20221125	59908.8	+52.1	NOT+ALFOSC	gm4+1″1	3500–9700	14	3600
20221126	59909.4	+52.7	COJ 2m+en12	red/blu+2″0	3500–10,000	13	3600
20221202	59915.2	+58.5	OGG 2m+en06	red/blu+2″0	3500–10,000	13	3600
20221215	59928.8	+72.1	NOT+ALFOSC	gm4+1″3	3500–9650	17	3600

Note.
[a] Phases are relative to r-band maximum light (MJD = 59856.7).

A.2. Photometric Data Reduction

All raw photometry images were first pre-reduced following the standard procedures in IRAF (D. Tody 1986, 1993), such as bias, overscan, and flat-field corrections. Multiple exposures were taken when the object was faint and then combined to increase the signal-to-noise ratio (S/N). The optical and NIR photometric data observed from ground-based telescopes were reduced using the dedicated pipeline *ecsnoopy*,[61] which comprises several photometric packages, such as SEXTRACTOR (E. Bertin & S. Arnouts 1996) for source extraction, DAOPHOT (P. B. Stetson 1987) for magnitude measurement through point-spread function (PSF) fitting, and HOTPANTS (A. Becker 2015) for image subtraction with PSF matching. The instrumental magnitudes of the SN are measured through the PSF-fitting technique, and calibrated against the catalogs of the A. U. Landolt (1992), Pan-STARRS, and the Two Micron All Sky Survey (2MASS; M. F. Skrutskie et al. 2006).

We retrieved the single exposure frames by the NEOWISE-Reactivation mission (E. L. Wright et al. 2010; A. Mainzer et al. 2014)—which scans the entire sky once every 6 months—from the IRSA Archive.[62] Then, we coadded them into a single image and performed the template subtraction using images acquired in 2014 May (8 yr before the explosion) as templates. The WISE magnitudes were calibrated against the WISE All-Sky Data Release catalog (R. M. Cutri et al. 2012). Swift/UVOT ultraviolet (UV) and optical photometry were retrieved from the NASA Swift Data Archive,[63] and measured using the standard UVOT data analysis software `HEASoft`[64](version 6.19, Nasa High Energy Astrophysics Science Archive Research Center Heasarc), along with the standard calibration data. The source flux is measured within a circular aperture of 5″. Sky background was computed in a manually chosen region with a radius of 25″.

The ZTF data were directly retrieved from the ZTF Forced Photometry Service (F. J. Masci et al. 2023), while the ATLAS light curves (K. W. Smith et al. 2020) were produced from the public Forced Photometry server[65](L. Shingles et al. 2021). Pan-STARRS (PS1+PS2) data were obtained through forced photometry on template-subtracted images following the similar method as in ATLAS dataset: in both cases, we stacked all measurements on a given day into a single measurement (for details of the Pan-STARRS transient survey data processing, see M. D. Fulton et al. 2025).

A.3. Spectroscopic Observation and Data Reduction

The classification spectrum (M. Fulton et al. 2022) was obtained with the University of Hawaii 2.2m telescope (UH88) plus the Supernova Integral Field Spectrograph (SNIFS) mounted on Maunakea, Hawaii, USA. The spectroscopic follow-up observations were carried out at the following facilities, including the X-Shooter spectrograph mounted on the 8.2 m Very Large Telescope (VLT) at the ESO Paranal observatory, Chile; the Lijiang 2.4 m Telescope (LJT) equipped with the Yunnan Faint Object Spectrograph and Camera (YFOSC; J.-G. Wang et al. 2023), located at Lijiang Observatory, China; the 4.1 m Southern Astrophysical Research Telescope (SOAR) with the Goodman High Throughput Spectrograph (GHTS) at Cerro Pachón in Chile; the Alhambra Faint Object Spectrograph and Camera (ALFOSC) on the NOT at the Observatorio del Roque de los Muchachos, La Palma, Spain, based on the Nordic Optical Telescope Unbiased Transient Survey 2 (NUTS2) project; the ESO Faint Object Spectrograph and Camera (EFOSC2) on the NTT at the La Silla Observatory, Chile, as part of the advanced Public ESO Spectroscopic Survey of Transient Objects (ePESSTO+) survey; the Las Cumbres Observatory (LCO; T. M. Brown et al. 2013) with a global telescope network located at different sites: the FLOYDS (en06) spectrograph on the OGG 2 m telescope at Haleakala Observatory, Maui, USA and the FLOYDS (en12) spectrograph on the COJ 2 m telescope at Siding Spring Observatory, NSW, Australia, which are part of the Global Supernova Project (GSP).

The spectra were reduced using routine IRAF tasks or with dedicated pipelines for specific instruments such as FOSC-GUI,[66] the PESSTO pipeline (S. J. Smartt et al. 2015), the SNIFS pipeline (M. A. Tucker et al. 2022), and the FLOYDS pipeline.[67] The different tools follow a standard manner: As a preliminary reduction, raw images were corrected for bias, overscan, trimming, and flat-fielding. Then, 1D spectra were optimally extracted from the 2D images. The wavelength calibration was performed using the arc-lamp spectra, while the flux of SN spectra was calibrated with the spectro-photometric standards. Both calibration images were taken during the same night as the SN observation. The flux calibrations of SN spectra were fine-tuned using the coeval broadband photometry, and finally major telluric absorption lines (e.g., from O_2 and H_2O) were removed from the SN spectra using the spectra of standard stars.

ORCID iDs

Y.-Z. Cai (蔡永志) https://orcid.org/0000-0002-7714-493X
A. Pastorello https://orcid.org/0000-0002-7259-4624
R. Chiba https://orcid.org/0009-0003-4594-3715
T. J. Moriya https://orcid.org/0000-0003-1169-1954
A. Reguitti https://orcid.org/0000-0003-4254-2724
L. Tartaglia https://orcid.org/0000-0003-3433-1492
S. Moran https://orcid.org/0000-0001-5221-0243
S. Campana https://orcid.org/0000-0001-6278-1576
Z.-Y. Wang https://orcid.org/0000-0002-0025-0179
J.-W. Zhao https://orcid.org/0009-0009-8633-8582
J. P. Anderson https://orcid.org/0000-0003-0227-3451
S. Benetti https://orcid.org/0000-0002-3256-0016
S. J. Brennan https://orcid.org/0000-0003-1325-6235
E. Cappellaro https://orcid.org/0000-0001-5008-8619
K. C. Chambers https://orcid.org/0000-0001-6965-7789
T.-W. Chen https://orcid.org/0000-0002-1066-6098
Y.-Z. Dong https://orcid.org/0000-0002-7937-6371
J. Duarte https://orcid.org/0000-0002-1823-3860

[61] *ecsnoopy* is a package for SN photometry using PSF fitting and/or template subtraction developed by E. Cappellaro. A package description can be found at http://sngroup.oapd.inaf.it/snoopy.html.
[62] https://irsa.ipac.caltech.edu/Missions/wise.html
[63] https://heasarc.gsfc.nasa.gov/cgi-bin/W3Browse/swift.pl
[64] https://heasarc.gsfc.nasa.gov/lheasoft/download.html
[65] https://fallingstar-data.com/forcedphot/
[66] Foscgui is a graphic user interface aimed at extracting SN spectroscopy and photometry obtained with FOSC-like instruments. It was developed by E. Cappellaro. A package description can be found at http://sngroup.oapd.inaf.it/foscgui.html.
[67] https://lco.global/documentation/data/floyds-pipeline/

N. Elias-Rosa https://orcid.org/0000-0002-1381-9125
M. Fraser https://orcid.org/0000-0003-2191-1674
W.-P. Gan https://orcid.org/0009-0007-7959-9288
H. Gao https://orcid.org/0000-0003-1015-5367
M. Gromadzki https://orcid.org/0000-0002-1650-1518
G. Hosseinzadeh https://orcid.org/0000-0002-0832-2974
D. A. Howell https://orcid.org/0000-0003-4253-656X
C. Inserra https://orcid.org/0000-0002-3968-4409
T. Kangas https://orcid.org/0000-0002-5477-0217
E. Kankare https://orcid.org/0000-0001-8257-3512
T. Kravtsov https://orcid.org/0000-0003-0955-9102
L.-P. Li https://orcid.org/0009-0003-3758-0598
C.-C. Lin https://orcid.org/0000-0002-7272-5129
T. B. Lowe https://orcid.org/0000-0002-9438-3617
P. Lundqvist https://orcid.org/0000-0002-3664-8082
E. A. Magnier https://orcid.org/0000-0002-7965-2815
K. Matilainen https://orcid.org/0000-0002-8111-4581
P. A. Mazzali https://orcid.org/0000-0001-6876-8284
C. McCully https://orcid.org/0000-0001-5807-7893
P. Minguez https://orcid.org/0009-0003-8803-8643
T. E. Müller-Bravo https://orcid.org/0000-0003-3939-7167
M. Newsome https://orcid.org/0000-0001-9570-0584
E. Padilla Gonzalez https://orcid.org/0000-0003-0209-9246
C. Pellegrino https://orcid.org/0000-0002-7472-1279
P. J. Pessi https://orcid.org/0000-0002-8041-8559
T. Petrushevska https://orcid.org/0000-0003-4743-1679
G. Pignata https://orcid.org/0000-0003-0006-0188
R. P. Santos https://orcid.org/0009-0002-2952-7431
S. Schulze https://orcid.org/0000-0001-6797-1889
S. J. Smartt https://orcid.org/0000-0002-8229-1731
I. A. Smith https://orcid.org/0000-0001-8605-5608
K. W. Smith https://orcid.org/0000-0001-9535-3199
J. Sollerman https://orcid.org/0000-0003-1546-6615
S. Srivastav https://orcid.org/0000-0003-4524-6883
M. D. Stritzinger https://orcid.org/0000-0002-5571-1833
G. Terreran https://orcid.org/0000-0003-0794-5982
G. Valerin https://orcid.org/0000-0002-3334-4585
R. Wainscoat https://orcid.org/0000-0002-1341-0952
S.-Q. Wang (王善钦) https://orcid.org/0000-0001-7867-9912
L. Galbany https://orcid.org/0000-0002-1296-6887
Z. Li https://orcid.org/0000-0003-0418-8461
I. Salmaso https://orcid.org/0000-0003-1450-0869
S. Zha (查帅) https://orcid.org/0000-0001-6773-7830
B. Wang (王博) https://orcid.org/0000-0002-3231-1167
X.-F. Wang (王晓锋) https://orcid.org/0000-0002-7334-2357
J.-J. Zhang (张居甲) https://orcid.org/0000-0002-8296-2590

References

Anderson, J. P., Habergham, S. M., James, P. A., & Hamuy, M. 2012, MNRAS, 424, 1372
Anupama, G. C., Sahu, D. K., Gurugubelli, U. K., et al. 2009, MNRAS, 392, 894
Astropy Collaboration, Price-Whelan, A. M., Sipőcz, B. M., et al. 2018, AJ, 156, 123
Astropy Collaboration, Robitaille, T. P., Tollerud, E. J., et al. 2013, A&A, 558, A33
Becker, A. 2015, HOTPANTS: High Order Transform of PSF ANd Template Subtraction, Astrophysics Source Code Library, ascl:1504.004
Bellm, E. C., Kulkarni, S. R., Graham, M. J., et al. 2019, PASP, 131, 018002
Bertin, E., & Arnouts, S. 1996, A&AS, 117, 393
Bianchi, L., Bohlin, R., & Massey, P. 2004, ApJ, 601, 228
Blinnikov, S. 2017, in Handbook of Supernovae, ed. A. W. Alsabti & P. Murdin (Springer International), 843
Boian, I., & Groh, J. H. 2019, A&A, 621, A109
Breeveld, A. A., Curran, P. A., Hoversten, E. A., et al. 2010, MNRAS, 406, 1687
Brennan, S. J., Fraser, M., Johansson, J., et al. 2022, MNRAS, 513, 5642
Brennan, S. J., Sollerman, J., Irani, I., et al. 2024, A&A, 684, L18
Brown, T. M., Baliber, N., Bianco, F. B., et al. 2013, PASP, 125, 1031
Burrows, D. N., Hill, J. E., Nousek, J. A., et al. 2005, SSRv, 120, 165
Cai, Y.-Z., Pastorello, A., Maeda, K., et al. 2026, A&A, 707, A157
Cardelli, J. A., Clayton, G. C., & Mathis, J. S. 1989, ApJ, 345, 245
Chambers, K. C., Magnier, E. A., Metcalfe, N., et al. 2016, arXiv:1612.05560
Chevalier, R. A. 1982, ApJ, 258, 790
Chevalier, R. A., & Fransson, C. 1994, ApJ, 420, 268
Chevalier, R. A., & Irwin, C. M. 2011, ApJL, 729, L6
Chiba, R., & Moriya, T. J. 2024, ApJ, 973, 14
Conti, P. S. 1975, MSRSL, 9, 193
Cutri, R. M., Wright, E. L., Conrow, T., et al. 2012, Explanatory Supplement to the WISE All-Sky Data Release Products,
Dastidar, R., Misra, K., Valenti, S., et al. 2025, A&A, 694, A260
De La Rosa, J., Roming, P., & Fryer, C. 2017, ApJ, 850, 133
Dessart, L. 2024, arXiv:2405.04259
Dessart, L., Audit, E., & Hillier, D. J. 2015, MNRAS, 449, 4304
Dessart, L., Hillier, D. J., & Kuncarayakti, H. 2022, A&A, 658, A130
Di Carlo, E., Corsi, C., Arkharov, A. A., et al. 2008, ApJ, 684, 471
Dilday, B., Howell, D. A., Cenko, S. B., et al. 2012, Sci, 337, 942
Dong, Y., Tsuna, D., Valenti, S., et al. 2024, ApJ, 977, 254
Elias-Rosa, N., Pastorello, A., Benetti, S., et al. 2016, MNRAS, 463, 3894
Farias, D., Gall, C., Narayan, G., et al. 2024, ApJ, 977, 152
Filippenko, A. V. 1997, ARA&A, 35, 309
Foley, R. J., Berger, E., Fox, O., et al. 2011, ApJ, 732, 32
Foley, R. J., Smith, N., Ganeshalingam, M., et al. 2007, ApJL, 657, L105
Fransson, C., Ergon, M., Challis, P. J., et al. 2014, ApJ, 797, 118
Fraser, M. 2020, RSOS, 7, 200467
Fraser, M., Inserra, C., Jerkstrand, A., et al. 2013, MNRAS, 433, 1312
Fraser, M., Stritzinger, M. D., Brennan, S. J., et al. 2021, arXiv:2108.07278
Fulton, M., Bulger, J., Huber, M. E., et al. 2022, TNSAN, 198, 1
Fulton, M. D., Smartt, S. J., Huber, M. E., et al. 2025, MNRAS, 542, 541
Gagliano, A., Villar, V. A., Matsumoto, T., et al. 2025, ApJ, 989, 182
Gangopadhyay, A. 2024, arXiv:2411.04107
Gangopadhyay, A., Dukiya, N., Moriya, T. J., et al. 2025, MNRAS, 537, 2898
Gehrels, N., Chincarini, G., Giommi, P., et al. 2004, ApJ, 611, 1005
Ginzburg, S., & Balberg, S. 2012, ApJ, 757, 178
Gorbikov, E., Gal-Yam, A., Ofek, E. O., et al. 2014, MNRAS, 443, 671
Graham, M. J., Kulkarni, S. R., Bellm, E. C., et al. 2019, PASP, 131, 078001
Hamuy, M., Phillips, M. M., Suntzeff, N. B., et al. 2003, Natur, 424, 651
Harris, C. R., Millman, K. J., van der Walt, S. J., et al. 2020, Natur, 585, 357
Hiramatsu, D., Berger, E., Gomez, S., et al. 2024a, arXiv:2411.07287
Hiramatsu, D., Matsumoto, T., Berger, E., et al. 2024b, ApJ, 964, 181
Hosseinzadeh, G., Arcavi, I., Valenti, S., et al. 2017, ApJ, 836, 158
Hosseinzadeh, G., McCully, C., Zabludoff, A. I., et al. 2019, ApJL, 871, L9
Hunter, J. D. 2007, CSE, 9, 90
Ivezić, Ž., Kahn, S. M., Tyson, J. A., et al. 2019, ApJ, 873, 111
Karamehmetoglu, E., Taddia, F., Sollerman, J., et al. 2017, A&A, 602, A93
Kiewe, M., Gal-Yam, A., Arcavi, I., et al. 2012, ApJ, 744, 10
Kuncarayakti, H., Anderson, J. P., Galbany, L., et al. 2018, A&A, 613, A35
Landolt, A. U. 1992, AJ, 104, 340
Maeda, K., & Moriya, T. J. 2022, ApJ, 927, 25
Mainzer, A., Bauer, J., Cutri, R. M., et al. 2014, ApJ, 792, 30
Martin, J. C., Hambsch, F. J., Margutti, R., et al. 2015, AJ, 149, 9
Masci, F. J., Laher, R. R., Rusholme, B., et al. 2023, arXiv:2305.16279
Matheson, T., Filippenko, A. V., Chornock, R., Leonard, D. C., & Li, W. 2000, AJ, 119, 2303
Mattila, S., Meikle, W. P. S., Lundqvist, P., et al. 2008, MNRAS, 389, 141
Matzner, C. D., & McKee, C. F. 1999, ApJ, 510, 379
Mauerhan, J. C., Smith, N., Filippenko, A. V., et al. 2013, MNRAS, 430, 1801
Metzger, B. D. 2022, ApJ, 932, 84
Modjaz, M., Li, W., Butler, N., et al. 2009, ApJ, 702, 226
Moriya, T. J., & Maeda, K. 2016, ApJ, 824, 100
Moriya, T. J., Maeda, K., Taddia, F., et al. 2013, MNRAS, 435, 1520
Moriya, T. J., Maeda, K., Taddia, F., et al. 2014, MNRAS, 439, 2917
Mould, J. R., Huchra, J. P., Freedman, W. L., et al. 2000, ApJ, 529, 786
Niblett, A. E., Fryer, D. A., & Fryer, C. L. 2025, ApJ, 994, 259
Niu, Z., Sun, N.-C., Zapartas, E., et al. 2026, ApJ, 1001, 44

Nyholm, A., Sollerman, J., Taddia, F., et al. 2017, A&A, 605, A6
Nyholm, A., Sollerman, J., Tartaglia, L., et al. 2020, A&A, 637, A73
Ofek, E. O., Sullivan, M., Cenko, S. B., et al. 2013, Natur, 494, 65
Pastorello, A., Benetti, S., Brown, P. J., et al. 2015b, MNRAS, 449, 1921
Pastorello, A., Cappellaro, E., Inserra, C., et al. 2013, ApJ, 767, 1
Pastorello, A., Kochanek, C. S., Fraser, M., et al. 2018, MNRAS, 474, 197
Pastorello, A., Mattila, S., Zampieri, L., et al. 2008a, MNRAS, 389, 113
Pastorello, A., Quimby, R. M., Smartt, S. J., et al. 2008b, MNRAS, 389, 131
Pastorello, A., Reguitti, A., Morales-Garoffolo, A., et al. 2019, A&A, 628, A93
Pastorello, A., Smartt, S. J., Mattila, S., et al. 2007, Natur, 447, 829
Pastorello, A., Wang, X. F., Ciabattari, F., et al. 2016, MNRAS, 456, 853
Pastorello, A., Wyrzykowski, Ł., Valenti, S., et al. 2015a, MNRAS, 449, 1941
Poole, T. S., Breeveld, A. A., Page, M. J., et al. 2008, MNRAS, 383, 627
Poznanski, D., Prochaska, J. X., & Bloom, J. S. 2012, MNRAS, 426, 1465
Ransome, C. L., & Villar, V. A. 2025, ApJ, 987, 13
Reguitti, A., Pastorello, A., Pignata, G., et al. 2019, MNRAS, 482, 2750
Reguitti, A., Pastorello, A., Pignata, G., et al. 2022, A&A, 662, L10
Reguitti, A., Pignata, G., Pastorello, A., et al. 2024, A&A, 686, A231
Roming, P. W. A., Kennedy, T. E., Mason, K. O., et al. 2005, SSRv, 120, 95
Salmaso, I., Cappellaro, E., Tartaglia, L., et al. 2025, A&A, 695, A29
Sanders, N. E., Soderberg, A. M., Foley, R. J., et al. 2013, ApJ, 769, 39
Schlafly, E. F., & Finkbeiner, D. P. 2011, ApJ, 737, 103
Schlegel, E. M. 1990, MNRAS, 244, 269
Schulze, S., Gal-Yam, A., Dessart, L., et al. 2025, Natur, 644, 634
Shingles, L., Smith, K. W., Young, D. R., et al. 2021, TNSAN, 7, 1
Shivvers, I., Zheng, W. K., Mauerhan, J., et al. 2016, MNRAS, 461, 3057
Silverman, J. M., Nugent, P. E., Gal-Yam, A., et al. 2013, ApJS, 207, 3
Skrutskie, M. F., Cutri, R. M., Stiening, R., et al. 2006, AJ, 131, 1163
Smartt, S. J., Chambers, K. C., Smith, K. W., et al. 2016, ApJL, 827, L40
Smartt, S. J., Valenti, S., Fraser, M., et al. 2015, A&A, 579, A40
Smith, K. W., Smartt, S. J., Young, D. R., et al. 2020, PASP, 132, 085002
Smith, N. 2014, ARA&A, 52, 487
Smith, N. 2017, in Interacting Supernovae: Types IIn and Ibn, ed. A. W. Alsabti & P. Murdin (Springer International), 403
Smith, N., Cenko, S. B., Butler, N., et al. 2012b, MNRAS, 420, 1135
Smith, N., Foley, R. J., & Filippenko, A. V. 2008, ApJ, 680, 568
Smith, N., Mauerhan, J. C., Silverman, J. M., et al. 2012a, MNRAS, 426, 1905
Smith, N., Miller, A., Li, W., et al. 2010, AJ, 139, 1451
Stetson, P. B. 1987, PASP, 99, 191
Stritzinger, M., Taddia, F., Fransson, C., et al. 2012, ApJ, 756, 173
Strotjohann, N. L., Ofek, E. O., Gal-Yam, A., et al. 2021, ApJ, 907, 99
Sun, N.-C., Maund, J. R., Hirai, R., Crowther, P. A., & Podsiadlowski, P. 2020, MNRAS, 491, 6000
Svirski, G., Nakar, E., & Sari, R. 2012, ApJ, 759, 108
Taddia, F., Stritzinger, M. D., Sollerman, J., et al. 2013, A&A, 555, A10
Tody, D. 1986, SPIE, 627, 733
Tody, D. 1993, ASPC, 52, 173
Tominaga, N., Limongi, M., Suzuki, T., et al. 2008, ApJ, 687, 1208
Tonry, J. L., Denneau, L., Flewelling, H., et al. 2018a, ApJ, 867, 105
Tonry, J. L., Denneau, L., Heinze, A. N., et al. 2018b, PASP, 130, 064505
Tsuna, D., Matsumoto, T., Wu, S. C., & Fuller, J. 2024, ApJ, 966, 30
Tucker, M. A., Shappee, B. J., Huber, M. E., et al. 2022, PASP, 134, 124502
Valenti, S., Sand, D., Pastorello, A., et al. 2014, MNRAS, 438, L101
Virtanen, P., Gommers, R., Oliphant, T. E., et al. 2020, NatMe, 17, 261
Walborn, N. R. 1977, ApJ, 215, 53
Walborn, N. R. 1982, ApJ, 256, 452
Wang, J.-G., Bai, J.-M., Zhao, Y.-H., et al. 2023, RAA, 23, 035014
Wang, S.-Q., & Li, L. 2020, ApJ, 900, 83
Wang, Z. Y., Pastorello, A., Maeda, K., et al. 2024, A&A, 691, A156
Wright, E. L., Eisenhardt, P. R. M., Mainzer, A. K., et al. 2010, AJ, 140, 1868